Full-Field Deformation Measurement and Crack Mapping on Confined Masonry Walls Using Digital Image Correlation

R. Ghorbani · F. Matta · M.A. Sutton

Abstract The understanding of the load-resistance mechanisms and failure modes of large-scale concrete and masonry structures relies on accurate measurements of surface motions and deformations, and faithful crack maps. Measurements are typically taken using surface-mounted point-wise sensors (PWSs), and crack maps are hand-drawn based on visual inspection. It is impractical to obtain detailed displacement and deformation maps that describe the complex response of large structures based on PWS measurements. In addition, manual crack drawing is difficult, time-consuming, and prone to human errors, which makes it challenging to consistently produce faithful crack maps. This paper reports on a pilot study to test the use of three-dimensional digital image correlation (3D-DIC) as a non-contacting method to measure surface deformation fields on full-scale masonry walls, and produce detailed crack maps. Three confined masonry walls were tested under horizontal in-plane reverse-cycle loads. The specimens were designed to attain different levels of strength and deformability through different load-resistance mechanisms. Representative 3D-DIC measurements of drift, diagonal deformations, and interface slip between the reinforced concrete tie columns and the masonry infill were evaluated vis-à-vis benchmark PWS measurements, showing a comparable accuracy. Strain maps based on 3D-DIC measurements were enlisted to visualize the development of the fundamental strut-and-tie resisting mechanism in confined masonry walls subjected to horizontal in-plane loads, and illustrate practical structural analysis and design implications. More detailed crack maps compared with traditional hand-drawn maps were obtained based on 3D-DIC maximum principal strain contours.

Keywords Crack mapping · Digital image correlation · Deformation measurement · Large-scale testing · Masonry structures · Seismic resistance

Introduction

The measurement of surface displacements, deformations and crack widths, and the mapping of surface cracks, are key to gain qualitative and quantitative information to understand the load-resistance mechanisms and failure modes of concrete and masonry structures. As the spatial resolution of these information increases, so does their value in informing the development of analysis and design algorithms as well as the verification and calibration of numerical models. In laboratory tests, displacements and deformations are traditionally measured using point-wise sensors (PWSs) such as linear potentiometers, crack opening gauges, and strain gauges [1–3]. However, PWSs provide local surface measurements with a set resolution, which can also be affected by the integrity of the PWS connections to the surface and random cracks forming near these connections or along the PWS gauge length. In addition, crack maps are typically hand-drawn at different loading (or displacement) steps or after failure. This practice is time-consuming and poses safety concerns especially when testing large-scale structures, and is highly

R. Ghorbani (SEM member)
Department of Civil and Environmental Engineering, University of South Carolina, 300 Main Street, Room B122A, Columbia, SC 29208, USA

F. Matta (✉, SEM member)
Department of Civil and Environmental Engineering, University of South Carolina, 300 Main Street, Room C210, Columbia, SC 29208, USA
e-mail: fmatta@sc.edu

M. Sutton (SEM fellow)
Department of Mechanical Engineering, University of South Carolina, 300 Main Street, Room A129, Columbia, SC 29208, USA

dependent on the personnel's skills in recognizing the presence and length of cracks, including elusive but relevant hairline cracks. Therefore, it is impractical to rely on PWSs to obtain detailed displacement and deformation maps, while manual crack drawing makes it challenging to produce faithful crack maps.

Three-dimensional (3D) digital image correlation (DIC) is poised to overcome these limitations. 3D-DIC combines subset-based DIC with stereo-vision to measure essentially full-field 3D surface motions [4, 5]. This measurement technique is based on a comparative analysis of digital images of patterned (i.e., having a random distribution of gray levels) surfaces. The images are acquired during the loading process using a calibrated stereo-vision system, which consists of a pair of rigidly-mounted digital cameras that are oriented to focus on the target surface. At each loading step, the 3D motion and deformation is extracted using a 3D-DIC software by selecting reference subsets in the undeformed state in one camera, extracting the matching image positions by comparing the reference subsets to those in the deformed image pairs, and performing triangulation between the matching subset centers in both cameras to locate the spatial position of the object point [4].

Subset-based 3D-DIC is attractive to complement measurements taken from inside concrete and masonry specimens (e.g., strain gauges mounted on reinforcing bars) with accurate surface deformation and crack maps. The goal is to gain new information to describe the load-resistance mechanisms and the progression of damage until failure, through a combination of size of the measurement area and spatial resolution that is unattainable with PWSs. This paper presents a pilot study on the use of 3D-DIC as a non-contacting method to accurately measure surface deformations on large masonry walls loaded in their plane, and produce faithful strain and crack maps to better describe the load-resistance mechanisms and damage evolution. Three full-scale confined masonry (CM) wall specimens were designed for different performance in terms of in-plane strength and deformability, and tested under reverse-cycle loads. The 3D-DIC test setup deployed is assessed by comparing relevant full-field displacement measurements with benchmark measurements performed with traditional contact-based displacement transducers. Then, the use of strain maps is demonstrated to visualize load-resistance mechanisms and crack maps, and discuss practical implications for structural analysis and design.

Challenges in Large-Scale Testing

There is little experience in performing DIC measurements on large-scale concrete and masonry structures [5], which present specific challenges. The first challenge is the design and application of high-contrast speckle patterns that ensure a suitable balance between measurement accuracy and spatial resolution. To maximize accuracy, the subset size used in the correlation analysis must be tailored to provide a distinctive intensity pattern to distinguish one subset from the others [6]. This is typically accomplished by using a speckle size between 2 and 5 pixels [7], and tailoring the subset size such that each subset contains at least 3×3 speckles [4]. However, the use of spray paint or toner powders may yield speckle patterns with a high-frequency content that cannot be captured with a standard-resolution (~2-6 megapixels) camera, resulting in aliasing problems. Conversely, the use of relatively large speckles, for example easily applied through manual painting, would result in reduced spatial resolution [8]. For the case of large masonry walls, suitable speckle patterns can be obtained on large (over 6 m^2), smoothed and whitewashed surfaces by spraying dark paint through flexible polymer stencils [9]. In the writers' experience, this approach is the most suitable as it consistently results in high-quality patterns, whereas the use of spackling brushes requires more practice and remains prone to inconsistent results, and direct painting of individual dots is viable but extremely time-consuming.

The second challenge is the setup of the stereo-vision system, with an emphasis on the selection of appropriate lenses and stereo angle [4]. To image a large surface, cameras with short focal length (wide-angle) need to be positioned at a relatively large distance from the specimen. Therefore, large-scale 3D-DIC tests call for sizable (e.g., 30 m^2 or more), unobstructed and uniformly-illuminated setup areas [9] whose suitability must be verified experimentally. The use of wide-angle lenses also results in an increase in the variability in 3D positions measured by image matching for image points that are located off the camera axis. This shortcoming can be offset by increasing the stereo angle (and thus the spacing between the cameras) to a maximum of 60°, whereas larger angles pose issues related to image foreshortening and loss of contrast [5, 10].

The third challenge is the effective calibration of the stereo-vision system, with an emphasis on lens distortion corrections. The process entails having both cameras observe a planar grid pattern placed on the target surface in different positions and orientations. Ideally, the grids should be sufficiently large to encompass a significant portion (e.g., one fourth) of the field of view, and sufficiently light to be manually moved so that cameras parameters, including distortion correction parameters, can be accurately determined. If smaller and easily movable grids are used on large surfaces, such as in this study, then assessing the measurement accuracy becomes especially important. In particular, more calibration images may be taken at the surface boundaries to quantify the effect of radial lens distortion, for which the associated measurement errors can be compensated for by using modern radial distortion models [11–13].

Previous Work

DIC techniques are becoming main-stream in experimental mechanics research using relatively small concrete and masonry specimens. In these instances, full-field deformation measurements proved especially useful to gain insight into complex mechanisms such as the delamination of externally bonded fiber-reinforced composite laminates [14–16]. Conversely, very few case studies on large-scale concrete and masonry structures have been reported in the literature, in part due to the challenges introduced in the previous section. These studies included DIC measurements on relatively small regions of interest (ROIs), and presented some quantitative comparisons between DIC and benchmark PWS measurements.

Lecompte et al. [17] enlisted a 3D-DIC system to monitor the surface deformations of a small ROI on the maximum tensile stress area of a prestressed concrete beam subjected to vertical cyclic loads. The spatial resolution allowed to recognize the position and extent of surface cracks based on maximum principal strain maps. Küntz et al. [18] used a 2D-DIC system to monitor a shear crack in a 245×190 mm ROI on a reinforced concrete (RC) beam of a bridge subjected to a diagnostic load test. The resulting displacement fields had a resolution of less than 10 μm, and offered comparable crack opening measurements to those of a benchmark linear potentiometer. However, the experiment highlighted the importance of applying a high-contrast speckle pattern (e.g., by painting or roughening the surface) as the insufficient contrast due to the lack of surface preparation allowed to analyzed only a 110×130 mm portion of the ROI. Destrebecq et al. [19] used a 2D-DIC system to monitor the surface deformations of a 718×102 mm ROI including the maximum tensile stress area of a large reinforced concrete (RC) beam subjected to vertical cyclic loads. Similar midspan deflections were measured compared with a benchmark linear variable differential transformer (LVDT) sensor, and it was shown that the technique holds potential to determine the location and width of tensile cracks based on horizontal displacement measurements. Tung et al. [20] used a 2D-DIC system with a $3,072 \times 2,048$ pixel camera to monitor the damage progression on the 400×300 mm surface of a 87 mm thick masonry wall with 45°-oriented mortar joints subjected to uniaxial compression, and on the $1,500 \times 1,200$ mm surface of a steel-framed masonry wall subjected to in-plane cyclic loading. A dark speckle pattern was spray-painted on a light background. It was shown that using Von Mises strain maps allowed to effectively recognize cracks based on a comparison with the result of visual inspections, and a better definition of crack positions and sizes was attained with smaller subsets (16×16 pixels instead of 32×32 pixels). Smith et al. [21] enlisted a 3D-DIC system to monitor the surface deformations of an approximately 1.3×1.0 m ROI at the base joint of a 0.4-scaled hybrid precast

concrete wall subjected to in-plane reverse-cycle loading. It was shown that DIC axial strain maps accurately depicted the damage progression at the joint, and DIC displacement measurements were comparable with those of PWSs for gap opening and shear distortion at the wall base, respectively. More recently, Guerrero et al. [22] demonstrated the use of DIC strain measurements to gain insight into the load-resistance mechanism (specifically, the angle of inclination of compressive struts) of full-scale masonry-infilled RC frames loaded horizontally in their plane. No assessment of the accuracy of DIC measurements was reported based on benchmark PWS measurements.

Experimental Program

Specimens and Materials

The test matrix included three full-scale CM wall specimens (SS, SA and SA-R) whose geometry, reinforcement layout and detailing are illustrated in Fig. 1 through Fig. 3. Each wall had width, height, and thickness of 2,430, 2,490, and 203 mm, respectively, and consisted of a RC frame (including two tie columns and a tie beam) that was cast on a $2,024 \times 2,235 \times 203$ mm masonry infill, and connected to a RC footing having width, height, and thickness of 3,556, 381, and 406 mm, respectively [Fig. 1(a)]. The masonry infills were constructed with hollow concrete masonry units (CMUs) having nominal dimensions of $200 \times 200 \times 400$ mm with a 50 % net cross-sectional area, and ordinary Portland cement (OPC) mortar consisting of three volume parts of sand, one part of Type N OPC, and water to ensure a slump of 150 mm. The CMUs were laid in a running bond pattern with bed and head joints having a thickness of approximately 10 mm. The RC tie columns and beams were constructed with Ø13 mm deformed Grade 60 steel bars and Ø6 mm deformed Grade 40 steel stirrups, and low-strength Type I OPC concrete. The salient strength properties of masonry and concrete materials are summarized in Table 1.

Each specimen was designed to attain a different level of in-plane strength and deformability at failure through different load-resistance mechanisms. Specimen SS is representative of a wall built with substandard ('S') details [Fig. 1(b)], including: column-beam connections with longitudinal bars terminating with short 180° hooked ends, which make the joints prone to premature failure due to the lack of tensile reinforcement resisting joint opening due to combined bending and shear; open stirrups with relatively large (203 mm) on-center spacing at both the column-beam and column-footing connections, reducing the effectiveness of the tie columns to resist shear forces and undergo large deformations without collapsing; and a smooth interface between RC tie columns and masonry infill, whose separation produced by in-plane loads

Fig. 1 Confined masonry specimens: (**a**) schematic; (**b**) detailing of specimen SS; and (**c**) detailing of specimens SA and SA-R for enhanced strength and deformability (note enhanced connections reinforcement and toothed interface between masonry panel and RC tie columns). Dimensions in mm
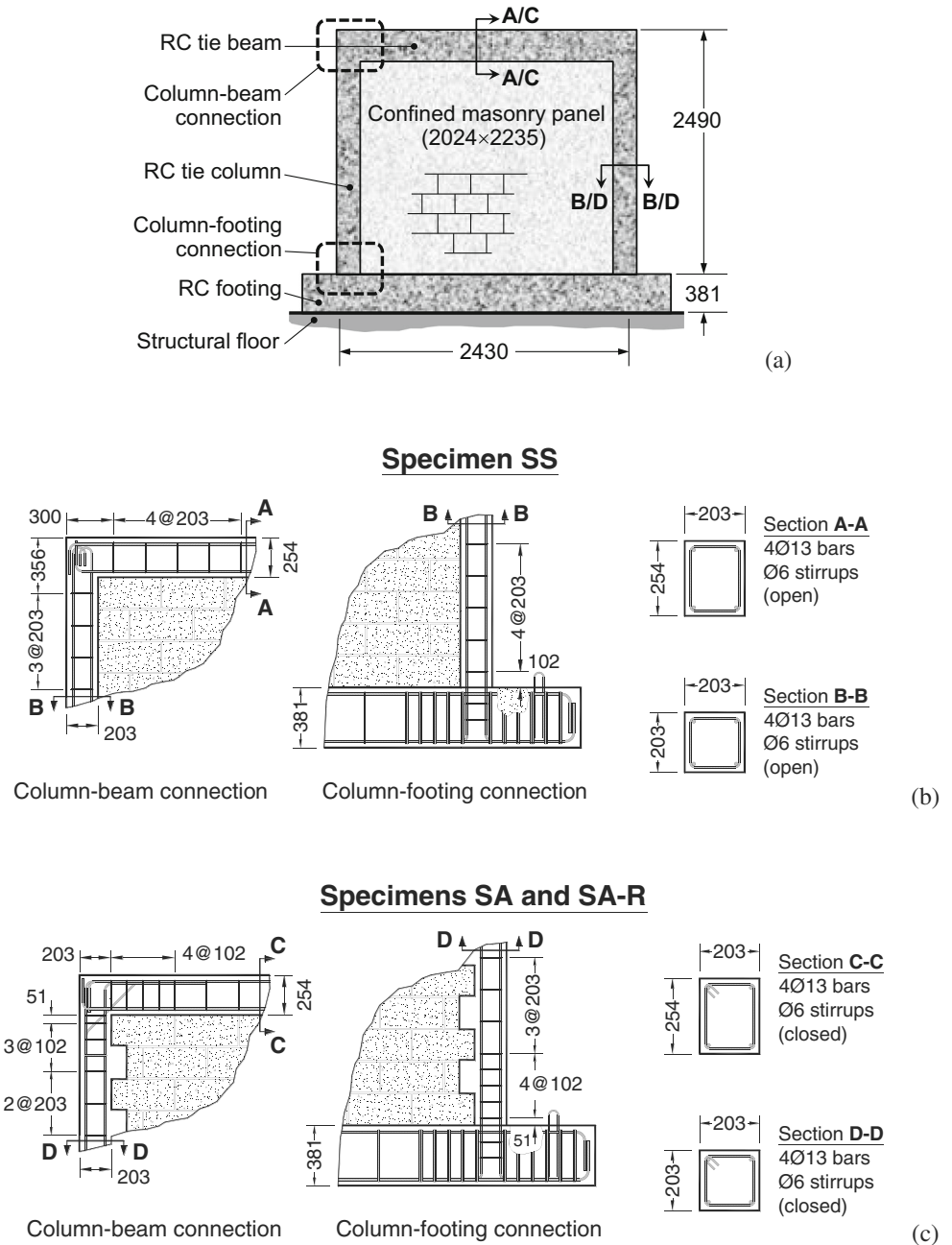
may negatively affect the strength and deformability of the CM wall.

Specimen SA is representative of a wall built with adequate ('A') details [Fig. 1(c)], including: column-beam connections tailored to resist the opening of the corner joint through longitudinal bars terminating with 90° bent ends having a length of 50 times the bar diameter to ensure an effective anchorage, and one well-anchored Ø13 mm diagonal steel bar; closed steel stirrups with a reduced (102 mm) on-center spacing at both the column-beam and column-footing connections; and a toothed masonry-RC interface to enhance the

mechanical interlocking between masonry infill and tie columns.

Specimen SA-R consisted of a SA wall that was retrofitted with aluminum strips embedded in the masonry bed joints to enhance in-plane strength and deformability, as illustrated in Fig. 2. The horizontal reinforcement included ten 6061-T6 aluminum strips having a cross section of 3.2×12.7 mm. Each strip was inserted in a saw-cut groove along a bed joint [Fig. 2(a)] and its 90° bent ends were anchored into pre-drilled slots in the RC tie columns [Fig. 2(b)], alternating from one face to the other face of

Table 1 Masonry and concrete material strength properties

Property	Test standard	Number of specimens	Average [MPa]	Standard deviation [MPa]
Concrete masonry units (CMU)				
Compressive strength	ASTM C140	6	7.2	0.29
Ordinary Portland cement mortar				
Compressive strength	ASTM C780	8	8.3	0.91
Masonry (CMU and mortar assemblies)				
Compressive strength	ASTM C1314	3	5.8	0.43
Flexural bond strength	ASTM E518	5	0.18	0.03
Shear strength	ASTM E519	3	0.32	0.02
Ordinary Portland cement concrete				
Compressive strength	ASTM C39	15	12.0	1.7
Splitting tensile strength	ASTM C496	8	1.2	0.13

Fig. 2 Horizontal reinforcement in specimen SA-R: (**a**) installation of aluminum strips in grooves cut along bed joints; and (**b**) close-up of reinforcement anchorage into RC tie column
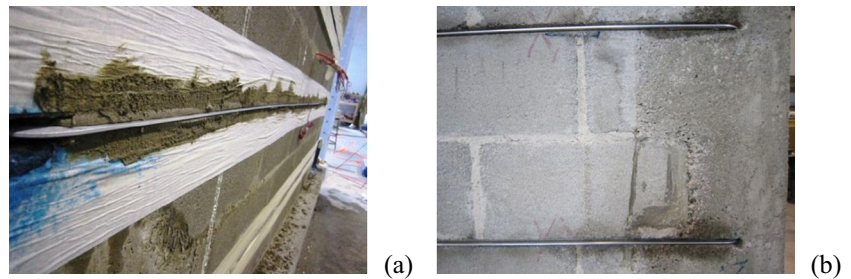
the wall. The reinforcement was then embedded in a conventional OPC mortar.

Test Setup and Instrumentation

Loading apparatus and point-wise sensors

The load test setup and PWS layout used for each specimen is shown in Fig. 3. The RC footing was tied to the structural floor using pre-tensioned steel threaded rods. The horizontal in-plane load was imparted using a hydraulic actuator with capacity of 500 kN and stroke of ±76 mm. The actuator had a swivel end bolted to a steel spreader beam that was rigidly connected to the top of the specimen RC tie beam by means of steel anchors. A constant vertical compression load of 88.3 kN was applied on top of the wall using a hydraulic jack and two steel spreader beams. The resulting uniformly distributed pressure of 0.2 MPa was intended to simulate the dead load of a second story.

The following PWSs were mounted on one face of each specimen (Fig. 3): (a) one linear potentiometer with stroke of ±76 mm and accuracy of ±0.08 %, labeled 'H1', which was connected to the top of the RC tie beam at its midspan and to an exterior fixed support, to measure the maximum horizontal

displacement (story drift); (b) two linear potentiometers with stroke of ±51 mm and accuracy of ±0.1 %, labeled 'D1' and 'D2', which were connected at the tie column-beam corners and at the base of the RC tie columns using 3 m aluminum extension rods, to measure diagonal deformations; and (c) two linear displacement transducers with stroke of ±25 mm and accuracy of ±0.35 %, labeled 'S1' and 'S2', which were connected to the tie columns at their midspan, to measure the differential displacement (slip) at the masonry-RC interface. Close-up photographs of the setup for sensors H1, D1 and S1 are shown in Fig. 4.
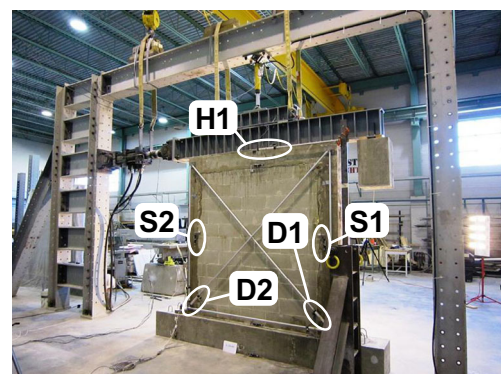

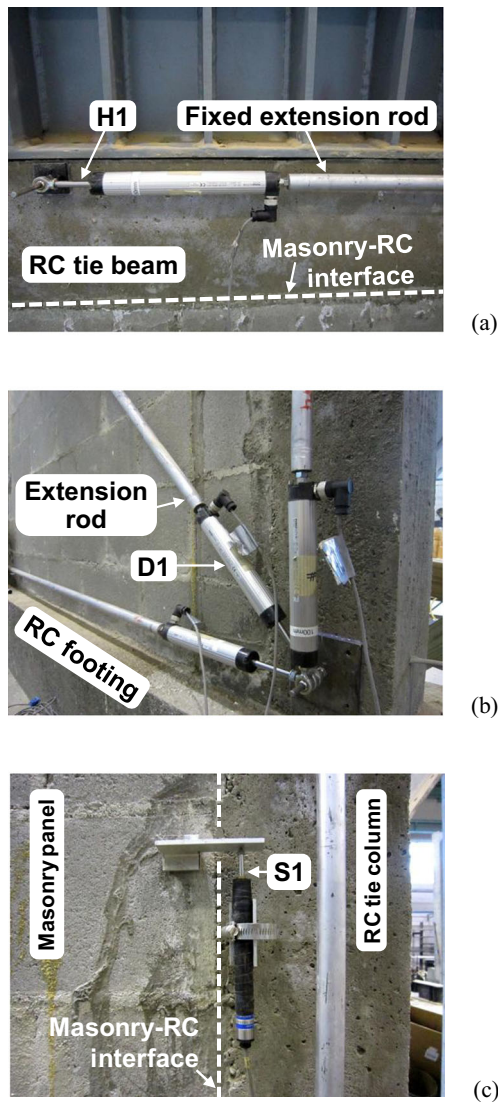**Fig. 3** Loading frame and point-wise sensor layout

Fig. 4 Close-up photographs of point-wise sensors: (**a**) H1; (**b**) D1; and (**c**) S1 at interface between RC tie column and masonry panel in specimen SS

Loading protocol

The in-plane reverse-cycle load, *V*, was imparted in displacement control mode following the sensor H1 displacement history in Fig. 5(a). For each displacement amplitude, three cycles were repeated at a frequency of 0.004 Hz. The third

cycle included two 30-s constant-displacement plateaus that served to capture images (30 per plateau) for 3D-DIC measurements [Fig. 5(b)]. This loading protocol aimed at accurately estimating the in-plane load-story drift (*V-d*) coordinates for three states that describe the mechanism of shear resistance of CM walls subjected to seismic loads, as illustrated in Fig. 6 [23]: (1) 'first crack' state, when diagonal cracking occurs in the masonry; (2) 'peak load' state, when the maximum load given by the combined shear strength of masonry infill and RC tie columns is attained, and the diagonal cracks propagate into the columns; and (3) 'ultimate' state, when the residual strength allows to attain the maximum drift before collapsing.

3D-DIC setup

The 3D-DIC setup presented in Fig. 7 was devised to meet the challenges illustrated earlier for measurements on large surfaces. The images were acquired with two CCD digital cameras having a 2,448×2,048 pixel resolution (Grasshopper GRAS-50S5M-C, Point Grey) and equipped with lenses with F-number of 1.4 and focal length of 17.6 mm (Xenoplan 1.4/ 17, Schneider). The cameras were mounted on a rigid crossbar and spaced 1.1 m apart. The crossbar was secured to a tripod, and the stereo-vision system was positioned at 6.7 m from the wall surface [Fig. 7(a)]. The relatively small stereo angle of 9.5° was considered acceptable as the main goal was to analyze in-plane rather than out-of-plane motions. Two banks of light-emitting diode (LED) lamps were used to illuminate the measurement surface. A desktop PC was used to store the images and analyze them through a 3D-DIC software (Vic- 3D, version 7, Correlated Solutions) [Fig. 7(b)]. The stereo- vision system was calibrated by taking 60 images of a calibration grid with different positions and orientations. The grid included 12×9 dots with nominal diameter of 20 mm and on- center spacing of 50 mm. The calibration results indicated that no lens distortion corrections were necessary, thus supporting the selected setup with respect to field of view, depth of field, and stereo-vision system components. During each load test, for each 30-s constant-displacement plateau in Fig. 5(b), 30 images were acquired to calculate average displacements and strains, thus minimizing measurement uncertainty.

Fig. 5 Loading protocol: (**a**) time-horizontal displacement (sensor H1) function; and (**b**) close-up showing sample constant displacement plateaus for image acquisition
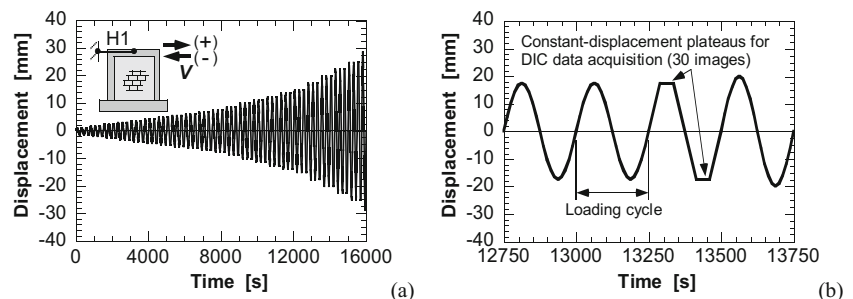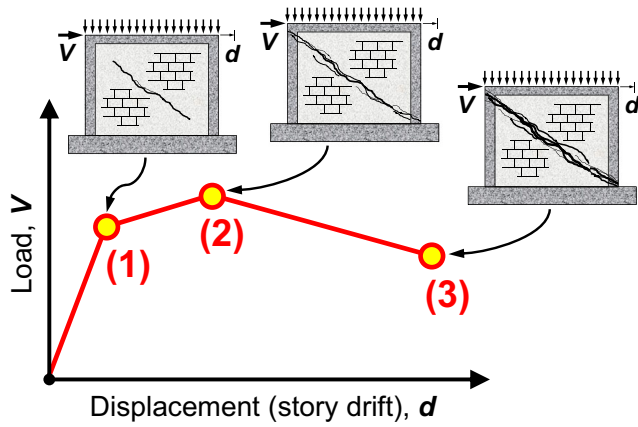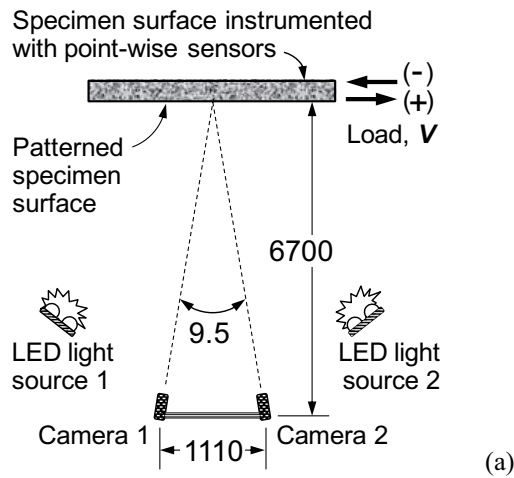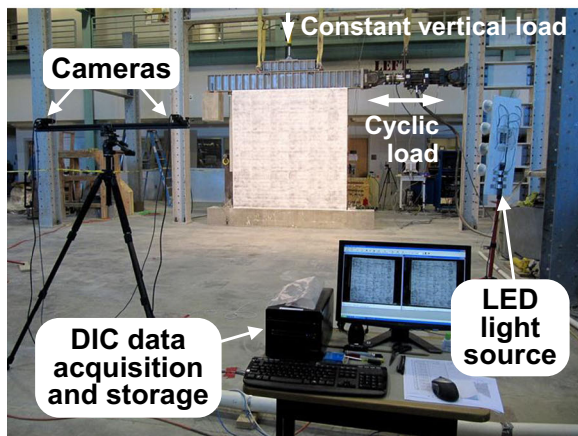
Fig. 6 Load resisting mechanism of CM wall under combined in-plane horizontal load, V (e.g., seismic load) and vertical load (e.g., weight of top floors and roof system) [23]: (*1*) diagonal cracking of masonry panel ('first crack' state); (*2*) propagation of diagonal cracks into RC tie columns at maximum load ('peak load' state); and (*3*) shear failure of masonry panel and RC tie columns ('ultimate' state)

Fig. 8 Spray-painting of speckle pattern on whitewashed background using stencil. Inset shows close-up view of finished pattern

Speckle pattern

The 2,430×2,490 mm surface of each CM wall was whitewashed, smoothed with sandpaper, and cleaned with a blow gun to create a light background. A dark speckle pattern was then spray-painted using a flexible polymer stencil placed against the wall surface, as shown in Fig. 8. The diameter of the speckles was approximately 3.2 mm, resulting in a speckle-to-surface area ratio of 33 %. Based on the field of view (3,330×2,790 mm) and camera resolution, each speckle was approximately 2.3 pixels in diameter. This approach was devised to address related challenges for large measurement surfaces by producing a high-quality pattern that offers good contrast and consistency throughout the region of interest and for different specimens, while being simple to apply. Fig. 9 shows the histogram of the gray levels in the speckle pattern for a representative portion of the surface of specimen SS, indicating a bell-shaped distribution that is suitable for DIC analysis.
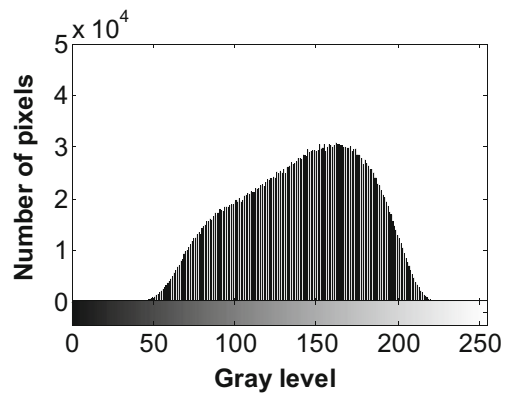

(a)

(b)

Fig. 7 3D-DIC setup: (**a**) schematic of plan view; and (**b**) photograph. Dimensions in mm

Fig. 9 Representative histogram of gray levels in speckle pattern (specimen SS)

Subset size for DIC analysis

The influence of subset size on the accuracy of displacement measurements was assessed by analyzing 31 images acquired from each unloaded specimen. One image was chosen as the reference, and the mean and standard deviation of the horizontal and vertical displacement components (*u* and *v*, respectively) for all data points were calculated to evaluate bias and standard deviation errors. A negligible change in bias was noted. Fig. 10(a) presents the standard deviation error ('STD') for *u* as a function of subset size for two representative specimens. The results show that the error decreases abruptly as the subset size increases. Since the tradeoff for enhanced accuracy is a reduced spatial resolution, a compromise was sought by selecting a 15×15 pixel subset size. This choice is also supported by the fact that each subset contains about 3×3 speckles [4] as shown in Fig. 10(b).

Results and Discussion

For each specimen, the in-plane load–displacement response is presented in Fig. 11. The positive (pull) and negative (push) load–displacement values (*V-d* in Fig. 6) at the first crack, peak load and ultimate state (~75-85 % of the peak load) are summarized in Table 2.

For specimen SS, failure was triggered by the opening of the column-beam joints after first cracking of the masonry infill due to the substandard joint reinforcement [Fig. 1(b)], resulting in little energy dissipation [Fig. 11(a)]. The improved detailing allowed specimen SA to attain a maximum increase in peak load and ultimate displacement of 18 and 73 %, respectively, compared with specimen SS, with a major enhancement in energy dissipation [Fig. 11(b)]. In particular, the use of diagonal Ø13 mm steel bars at the column-beam joints [Fig. 11(c)] offset the opening of the corner joints at increasing drifts. The main effect was to enable the development of the typical 'strut-and-tie' resisting mechanism of CM walls as the masonry infill acted as a diagonal strut resisting compression

forces, and the RC tie columns resisted primarily axial forces (tension or compression, depending on the direction of the horizontal load) [23] until diagonal cracking failure of the CM wall occurred. For specimen SA-R, the additional reinforcement embedded in the bed joints and anchored in the RC tie columns (Fig. 2) contributed by offsetting the opening of diagonal cracks and their propagation into the columns, resulting in a maximum increase in peak load and ultimate displacement of 19 and 23 %, respectively, compared with specimen SA, and further enhancing energy dissipation [Fig. 11(c)]. These results show that three different performance levels were attained, consistent with the objectives set forth in the design of the specimens. In the following sections, the results of 3D-DIC analysis are discussed based on displacement measurements, full-field strain maps, crack maps, and practical implications for structural analysis and design.
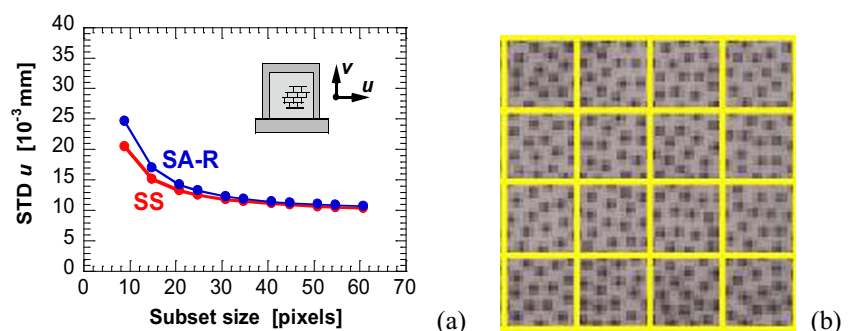
Displacement Measurements

To compare the 3D-DIC measurements of in-plane horizontal displacement, diagonal deformation, and interface slip, with those from PWSs, the motions of the points on the patterned surface [Fig. 7(b)] corresponding to those monitored with PWSs on the opposite surface (Fig. 3) were considered.

Horizontal displacement The drift measurements from sensor H1 [Fig. 3 and Fig. 4(a)] are compared with their 3D-DIC counterparts in the load-drift envelopes in Fig. 12, which are derived from the hysteretic curves in Fig. 11. The maximum standard deviation for the 30-image sets analyzed was ±15 μm (~ ±0.01 pixels), confirming the validity of the 3D-DIC setup deployed. It is noted that for all specimens the DIC measurements consistently mark similar envelopes to those of sensor H1, irrespective of the load direction and displacement level. To enable a quantitative comparison, the percent difference, Δ, between DIC and PWS measurements, δ_{DIC} and δ_{PWS}, was calculated via equation (1) for any given constant-displacement plateau point in Fig. 5(b):

$$\Delta = \left| \frac{\delta_{DIC} - \delta_{PWS}}{\delta_{PWS}} \right| \times 100\% \tag{1}$$

Fig. 10 Selection of subset size: (**a**) standard deviation error for horizontal displacement, *u*, as function of subset size at zero load for specimens SS and SA-R; and (**b**) 15×15 pixel subset size compared with speckle pattern
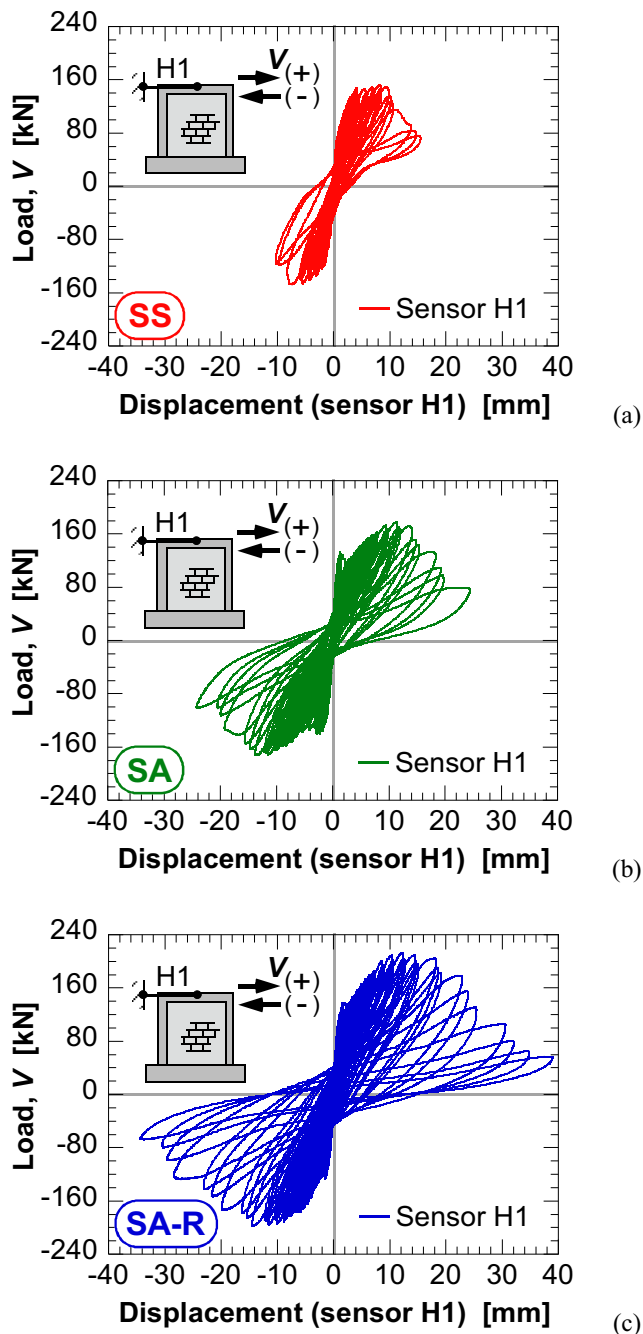
Fig. 11 Hysteretic load–displacement response based on sensor H1 measurements: (**a**) specimen SS; (**b**) specimen SA; and (**c**) specimen SA-R

Table 2 Summary of cyclic load test results

Specimen	'First crack' state		'Peak load' state		'Ultimate' state	
	V [kN]	d [mm]	V [kN]	d [mm]	V [kN]	d [mm]
SS	+107	+1.7	+152	+8.3	+115	+11.0
	−118	−1.5	−148	−7.4	−116	−10.2
SA	+132	+1.4	+179	+11.6	+133	+18.3
	−135	−1.8	−172	−13.7	−141	−17.7
SA-R	+137	+2.0	+213	+12.2	+179	+22.5
	−125	−1.5	−197	−14.3	−153	−21.5

fact that 3D-DIC measurements attained a comparable accuracy to PWS measurements indicates that the DIC setup and analysis approach were effective in meeting the challenges posed by the large measurement surfaces. This conclusion is reinforced by the results of diagonal deformation and interface slip measurements discussed below. In addition, this evidence supports the hypothesis that the full hysteretic response can be traced using 3D-DIC measurements without using surface-mounted PWSs, provided that images are acquired continuously, and possibly without the need of constant-displacement plateaus [Fig. 5(b)].

Diagonal deformation The measurements from sensor D1 [Fig. 3 and Fig. 4(b)] are compared with their 3D-DIC counterparts in the load-diagonal displacement envelopes in Fig. 14. The maximum standard deviation for the 30-image sets analyzed was ±45 μm (~ ±0.03 pixels). This value is higher than for the horizontal displacements, reflecting the fact that diagonal deformation measurements are more susceptible due to the effect of random cracks developing along and across the gauge length. This issue also applies to PWS measurements, in addition to the effect of vibrations of relatively long extension rods (in this case, 3 m). For all specimens, the DIC measurements consistently mark similar envelopes to those of sensor D1 in both elongation and contraction. The percent difference between DIC and PWS measurements was calculated per equation. (1) and, for each specimen, is plotted in Fig. 15 as a function of the positive and negative displacements measured through sensor D1. Such difference, Δ, rapidly reduces to less than 10 % (and typically below 6 %) after first cracking. Again, 3D-DIC measurements offered a comparable accuracy to those of the counterpart PWS.

Interface slip The slip between masonry infill and RC tie columns is an important indicator of the integrity of CM walls subjected to in-plane shear forces, especially when non-toothed interfaces are used as in the case of specimen SS [Fig. 1(b)]. The time-history of sensor S1 [Fig. 3 and Fig. 4(c)] measurements for specimen SS is plotted in

Δ is plotted in Fig. 13 as a function of the positive and negative drifts measured through sensor H1. The vertical dashed lines mark the displacement levels associated with first crack, peak load, and ultimate state (Table 2). For all specimens, the measurement difference rapidly reduces to less than 4 % after the formation of the first shear crack, that is, as the load-resistance mechanisms of interest to assess the strength and deformability of a seismic-resistant CM wall develop. The
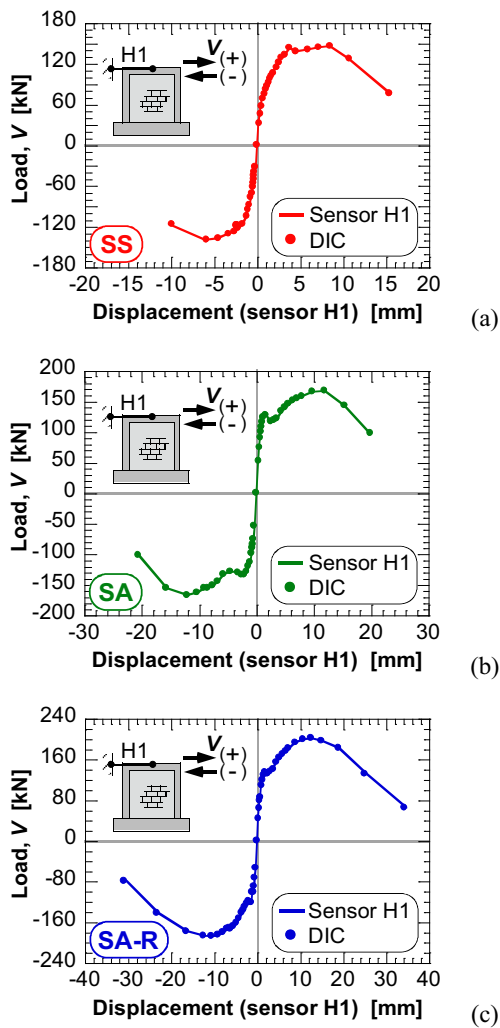
Fig. 12 Comparison between displacement measurements through sensor H1 and 3D-DIC based on load–displacement envelopes: (a) specimen SS; (b) specimen SA; and (c) specimen SA-R
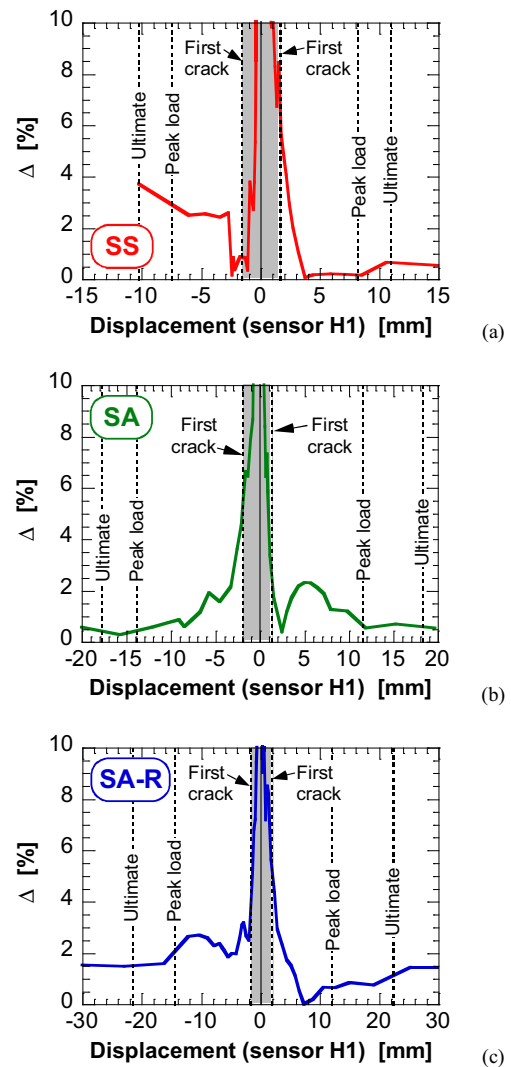

Fig. 13 Measurement difference between sensor H1 and 3D-DIC within range of positive and negative displacement at ultimate state: (a) specimen SS; (b) specimen SA; and (c) specimen SA-R

Fig. 16(a) vis-à-vis the horizontal in-plane load. A negligible slip is noted at any given load level. Fig. 16(b) presents the 3D-DIC vertical displacement profile along an 80-mm long reference line (including 200 data points), which lies perpendicular to the masonry-RC interface at the patterned location opposite to that of sensor S1. There are negligible discontinuities (i.e., slip) along the displacement profiles irrespective of the load level, in agreement with the measurements from sensor S1. This evidence suggests that 3D-DIC measurements can be used in lieu of PWS ones, whose accuracy is especially sensitive to the presence of random cracks in the tie columns near the sensor connection. In addition, 3D-DIC slip measurements can be made anywhere along the masonry-RC interfaces, offering a far more versatile assessment tool that capitalizes on the full-field nature of DIC measurements. From a practical standpoint, the absence of interface slip indicates that the masonry infill acted monolithically with the RC frame, which is a fundamentally different behavior from RC frames

with masonry infills where the masonry contributes to the load-resistance mechanism only under relatively large drifts due to the presence of interface gaps. In particular, for the case of specimen SS, the lack of interface slip highlights the negligible benefit to strength and deformability of using a toothed instead of a non-toothed interface, contrary to popular belief, and emphasizes the predominant importance of a suitable reinforcement detailing in the RC column-beam joints.

Full-Field Strain Maps

Full-field strain maps were derived from the measured 3D-DIC in-plane motions to gain an insight into the hypothetical strut-and-tie load-resistance mechanism [23] governing shear strength and deformability. Fig. 17 shows the positive in-plane load-drift envelope for each specimen, where the markers
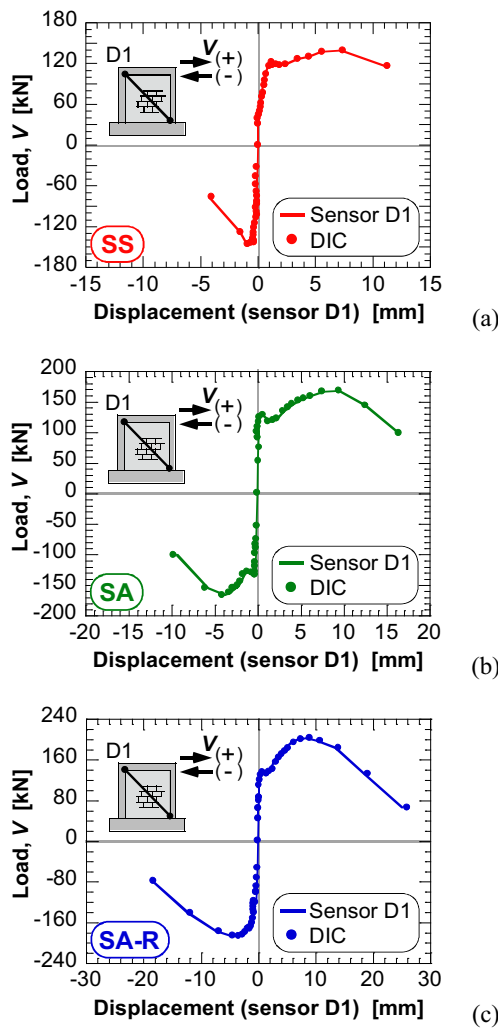
Fig. 14 Comparison between displacement measurements through sensor D1 and 3D-DIC based on load–displacement envelopes: (**a**) specimen SS; (**b**) specimen SA; and (**c**) specimen SA-R
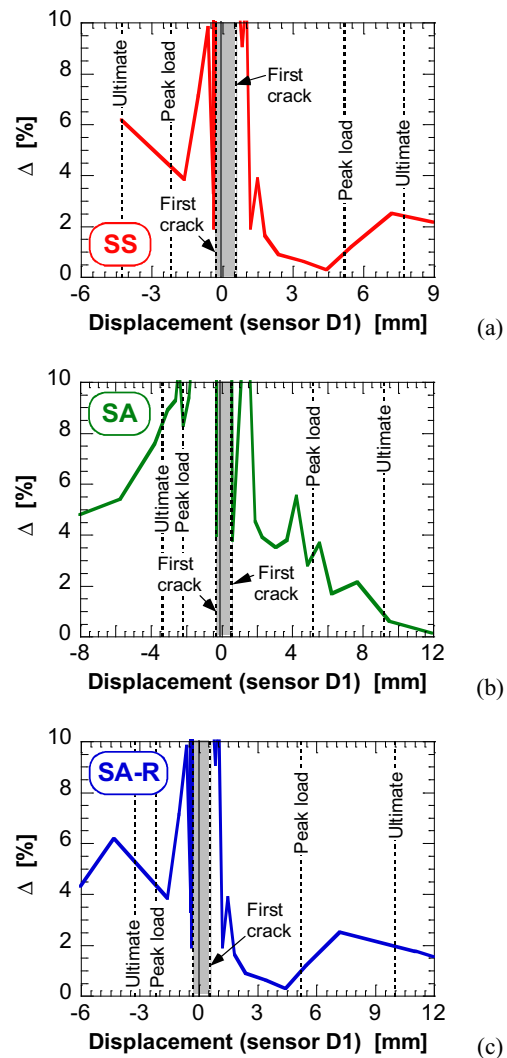

Fig. 15 Measurement difference between sensor D1 and 3D-DIC within range of positive and negative displacement at ultimate state: (**a**) specimen SS; (**b**) specimen SA; and (**c**) specimen SA-R

indicate representative points including: (A) uncracked state; (B) first crack state; (C) increasing load past the first crack state and before reaching the peak load; (D) peak load state; and (E) ultimate state. For each of these points, Fig. 18, Fig. 19, and Fig. 20 present the 3D-DIC map of the strain component parallel to the hypothetical compression strut in the masonry infill, ε_X, for specimens SS, SA, and SA-R, respectively.

In specimen SS, the ε_X contours indicate the progressive development of a compression strut along the X-direction once the first diagonal crack formed close to the wall base in point (B), at a load $V=+107$ kN and drift $d=1.7$ mm, together with flexural cracks along the left RC tie column (Fig. 18). The strut is visualized through the ~ -500 μm/m negative strain contours. The cracks are visualized as narrow discontinuity regions with positive (tensile) strain peaks of the order of 10^3 μm/m. The compression strut degrades after reaching the peak load of +152 kN in point

(D) until failure occurs due to the opening of the left column-beam joint. The 3D-DIC ε_X map provides compelling visual evidence that the strength of the diagonal compression strut in the masonry, which is expected to form in well-functioning CM walls [23], was not exploited. In fact, the limited diagonal cracking indicates that this mechanism did not fully develop due to the premature opening of the column-beam joint, resulting in a significantly smaller strength, deformability, and energy dissipation compared with specimens SA and SA-R. This observation is confirmed in Fig. 21, which shows the 3D-DIC map of the strain along the other diagonal, ε_Y, at the negative (push) peak load state for specimens SS, SA, and SA-R. The maps clearly show a less developed compression strut in specimen SS.

The 3D-DIC ε_X and ε_Y strain contours for specimen SA (Fig. 19 and Fig. 21) explain the enhanced hysteretic response
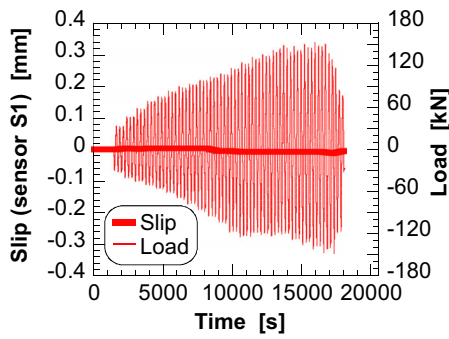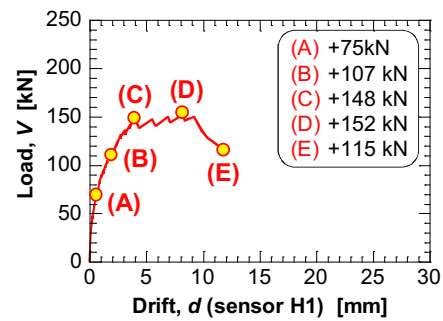
Fig. 16 Interface slip between masonry panel and RC tie column in specimen SS: (a) slip measured through sensor S1 vis-à-vis loading history; and (b) 3D-DIC vertical displacement profile along virtual line EF across masonry-RC interface at different load-drift (V-d) levels

in Fig. 11(b). In fact, the formation of well-defined diagonal compression struts was enabled by the resistance of column-beam joints against opening. The strain maps offer comprehensive visual evidence up to the ultimate state ($V<+133$ kN, $d<18.3$ mm), where the DIC analysis cannot be performed on the patterned areas where extensive spalling of the masonry infill occurred (Fig. 19).

The effectiveness of 3D-DIC measurements is further demonstrated in the case of specimen SA-R. First, the ε_X and ε_Y strain contours in Fig. 20 and Fig. 21 visualize the development of the compression strut past the first crack state ($V=+137$ kN, $d=2.0$ mm). Then, the crack-bridging contribution of the bed-joint reinforcement (Fig. 2) is rendered in the widening of the compression struts (ε_X and $\varepsilon_Y\sim-500$ μm/m) involving nearly the entire diagonal length of the masonry infill at the peak load state and under the large drifts attained at the ultimate state [Fig. 11(c)].

To the best of the writers' knowledge, this study is the first to systematically validate 3D-DIC measurements on full-scale masonry structures vis-à-vis PWS measurements, and demonstrate the visualization of a strut-and-tie and shear-resistance mechanism based on full-field deformation measurements. In particular, the strut-and-tie mechanism was originally hypothesized by Polyakov in 1956 [24] and Holmes in 1961 [25] for masonry infills, and became the theoretical foundation for the in-plane strength analysis of masory-infilled RC frames as
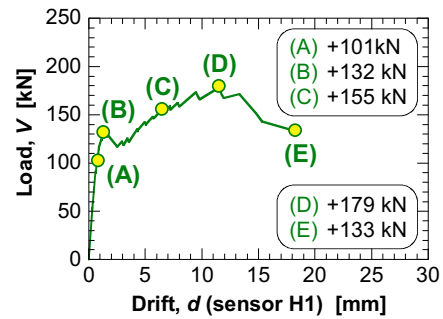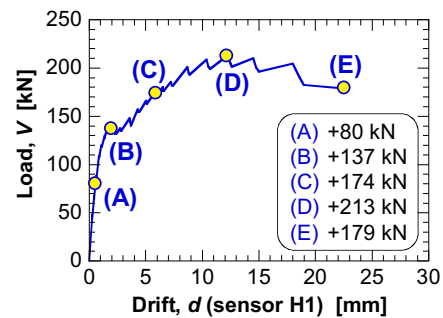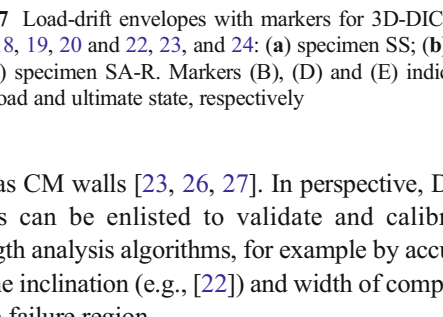
Fig. 17 Load-drift envelopes with markers for 3D-DIC strain maps in Figs. 18, 19, 20 and 22, 23, and 24: (a) specimen SS; (b) specimen SA; and (c) specimen SA-R. Markers (B), (D) and (E) indicate first crack, peak load and ultimate state, respectively

well as CM walls [23, 26, 27]. In perspective, DIC measurements can be enlisted to validate and calibrate existing strength analysis algorithms, for example by accurately defining the inclination (e.g., [22]) and width of compression struts in the failure region.

Full-Field Crack Maps

3D-DIC strain maps were also evaluated to understand the feasibility of producing faithful crack maps at different loading stages. The spatial resolution of DIC measurements is influenced primarily by the subset size used in the correlation analysis [8]. The selection of a 15×15 pixel subset size as a reasonable compromise between accuracy and resolution (Fig. 10) is further supported in Fig. 22(a), Fig. 23(a) and Fig. 24(a), which present the 3D-DIC crack
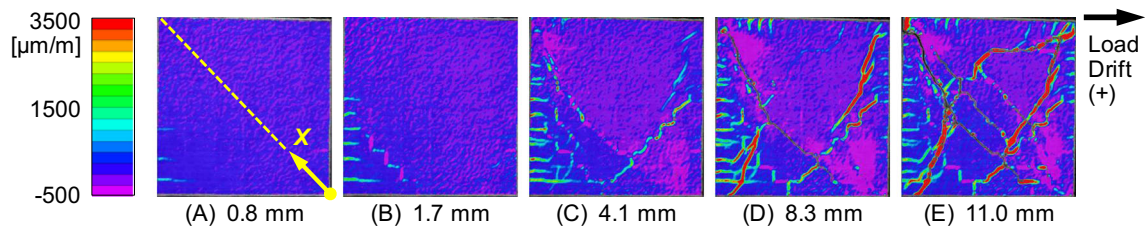
Fig. 18 DIC ε_X maps at increasing positive drift (sensor H1) in specimen SS ($\varepsilon_X<0$ indicates compression)

maps based on the maximum principal strain, ε_1, at the first crack, peak load, and ultimate state under positive load for specimens SS, SA and SA-R, respectively. For all specimens, the discontinuities indicating open cracks are marked by ε_1 with peak values on the order of 10^3 μm/m, thus well above those associated with masonry and concrete cracking ($\sim10^2$ μm/m).

The 3D-DIC ε_1 maps visualize the flexural cracks that formed horizontally on the left RC tie column and propagated into the masonry infill at the first crack state. For specimen SS, the limited energy dissipation [Fig. 11(a)] is described by the rapid opening of the left column-beam joint once the peak load was attained ($V=+152$ kN, $d=8.3$ mm), resulting in a limited development of diagonal cracks between the peak load and ultimate state, until the joint failed [Fig. 22(a)]. For specimen SA, the enhanced joint reinforcement [Fig. 1(c)] resulted in significantly higher strength and deformability than specimen SS [Fig. 11(b)] with comparable diagonal cracks at the peak load and ultimate state [Fig. 23(a)]. For specimen SA-R, the denser ε_1-based crack maps at the peak load and ultimate state highlight the contribution of the

additional bed-joint reinforcement (Fig. 2) in further enhancing strength and deformability [Fig. 11(c)]. In fact, multiple diagonal cracks formed due to the crack-bridging action exerted by the reinforcement, and the entire upper half of the masonry infill was involved in the load-resistance mechanism [Fig. 24(a)]. From a practical standpoint, the evidence provided through 3D-DIC strain maps can be used to define the amount and location of bed-joint reinforcement, and verify the effectiveness of these design choices, irrespective of the specific type of masonry structure (e.g., confined or infilled). For example, in the case of specimen SA-R, the limited damage developing in the lower third of the masonry infill suggests that reinforcement is needed primarily in the top two thirds, whereas reinforcement used elsewhere may not significantly contribute to strength and deformability. This consideration is especially important when designing seismic-resistant strengthening or repair systems because prescribing redundant reinforcement entails more time-consuming and labor-intensive construction operations, with a negative impact on typically stringent time and budget constraints.
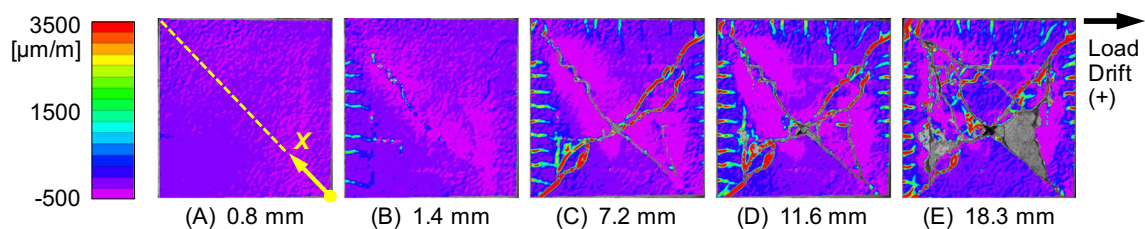

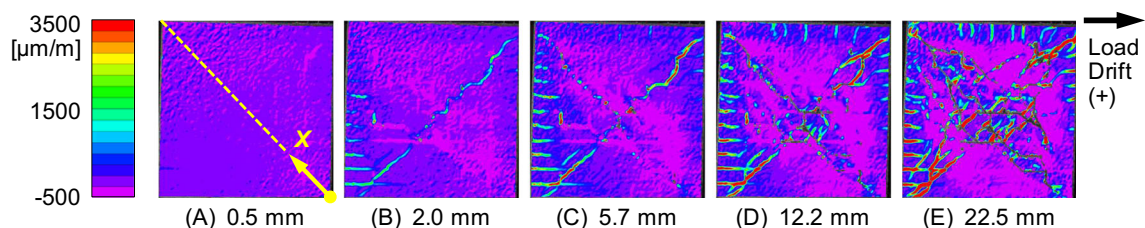**Fig. 19** DIC ε_X maps at increasing positive drift (sensor H1) in specimen SA ($\varepsilon_X<0$ indicates compression)

Fig. 20 DIC ε_X maps at increasing positive drift (sensor H1) in specimen SA-R ($\varepsilon_X<0$ indicates compression)

Fig. 21 DIC ε_Y maps at negative peak load in specimens SS, SA and SA-R ($\varepsilon_Y < 0$ indicates compression)
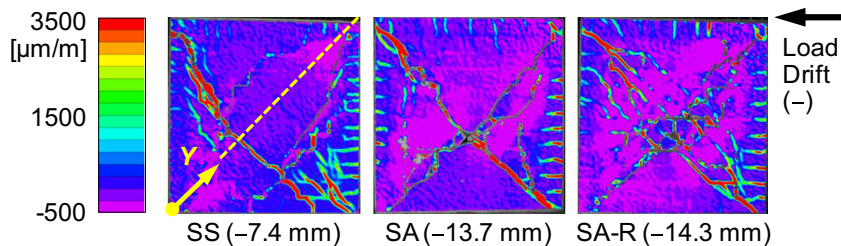

Fig. 22(b), Fig. 23(b) and Fig. 24(b) show the final hand-drawn crack maps from the opposite face of each specimen, which were mirrored (left-right) to facilitate the comparison with their DIC counterparts. Comparing 3D-DIC with hand-drawn crack maps in Fig. 22, Fig. 23 and Fig. 24 shows that more detailed maps are obtained through non-contacting DIC measurements. In particular, for all specimens the hand-drawn maps do not indicate most of the damage highlighted by the DIC maps along the RC tie beam, including the column-beam joints. Human error is inevitably a factor. However, it is noted that for safety purposes hand-drawn maps were made on unloaded specimens after failure, when most of the cracks in the concrete were closed with the exception of the failed left corner in specimen SS (Fig. 22), and thus were difficult to recognize. This is not a concern for DIC maps as they are based on ε_1

values derived from displacements measured on loaded specimens, when the cracks were open. The evidence presented indicates that faithful 3D-DIC crack maps can be obtained, with the following advantages over hand-drawn maps: (a) better level of detail, especially for closing cracks; (b) minimized influence of human errors; (c) ability to map cracks at any loading stage, thereby enabling one to monitor damage formation and development, which is impractical otherwise; and (d) safety, as non-contacting measurements are made without the need to closely inspect brittle specimens approaching collapse. In particular, the ability to map damage progression in a full-field fashion and at different loading stages makes 3D-DIC measurements an attractive means to obtain valid experimental evidence to underpin the verification and calibration of numerical (e.g., finite element) models.
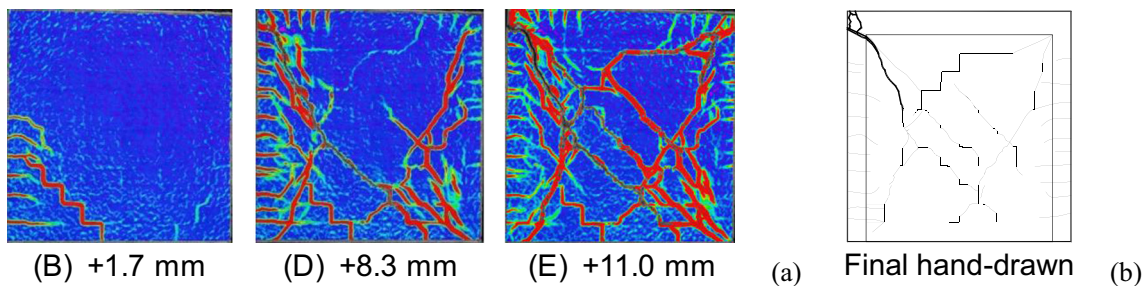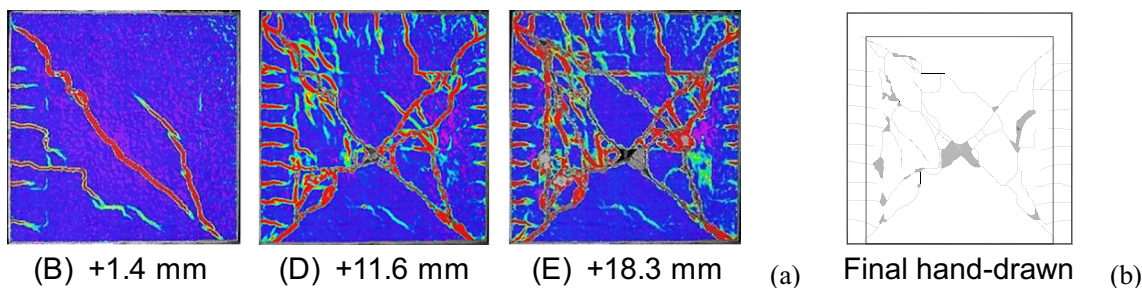

Fig. 22 Crack mapping on specimen SS: (**a**) DIC maximum principal strain map at first crack (B), peak load (D), and ultimate (E) state using 15×15 pixel subsets. Displacement values indicate drift per sensor H1; and (**b**) hand-drawn maps based on visual inspection. Red corresponds to +3,000 μm/m
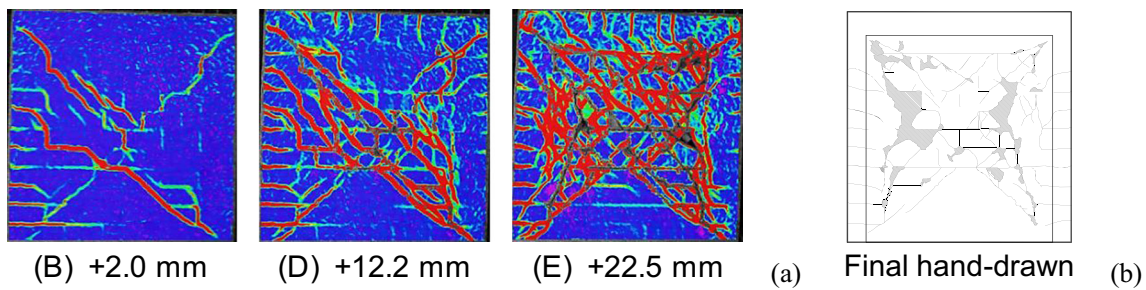

Fig. 23 Crack mapping on specimen SA: (**a**) DIC maximum principal strain map at first crack (B), peak load (D), and ultimate (E) state using 15×15 pixel subsets. Displacement values indicate drift per sensor H1; and (**b**) hand-drawn maps based on visual inspection. Red corresponds to +3,000 μm/m

Fig. 24 Crack mapping on specimen SA-R: (a) DIC maximum principal strain map at first crack (B), peak load (D), and ultimate (E) state using 15×15 pixel subsets. Displacement values indicate drift per sensor H1; and (b) hand-drawn maps based on visual inspection. Red corresponds to +3,000 μm/m

Potential for Crack Width Calculation

The potential to estimate crack widths through the analysis of 3D-DIC displacement measurement is illustrated in Fig. 25. Fig. 25(a) shows the DIC vertical displacement map for specimen SA-R at the positive peak load state (V=+213 kN, d=12.2 mm), marking line GH that intersects multiple flexural (horizontal) cracks along the left RC tie column. In Fig. 25(b), the vertical displacement profiles along line GH are plotted for different positive load levels vis-à-vis the interested portion of the ε_1-based crack map at V=+213 kN. It is noted that the discontinuities in the vertical displacement profiles indicate the open cracks along line GH. These evidence suggests that the amplitude of the discontinuities provides a measure of crack width as it increases at increasing drifts up to the ultimate state (V=+179 kN, d=22.5 mm), thus capturing the progressive opening of the tensile cracks along the tie column. This outcome is similar to that presented by Destrebecq et al. [19] for the case of tensile cracks in the constant moment region of a RC beam. However, experiments where progressive crack openings are locally measured with benchmark PWSs (e.g., crack opening gauges) are needed to test if and how the amplitude of the discontinuities in a given displacement profile can be used to accurately estimate crack widths.

Fig. 25 Potential to estimate crack widths in specimen SA-R: (a) vertical displacement map at peak load; and (b) maximum principal strain map at peak load vis-à-vis vertical displacement profile along line GH at different positive loads, V, showing progressive crack opening in RC tie column
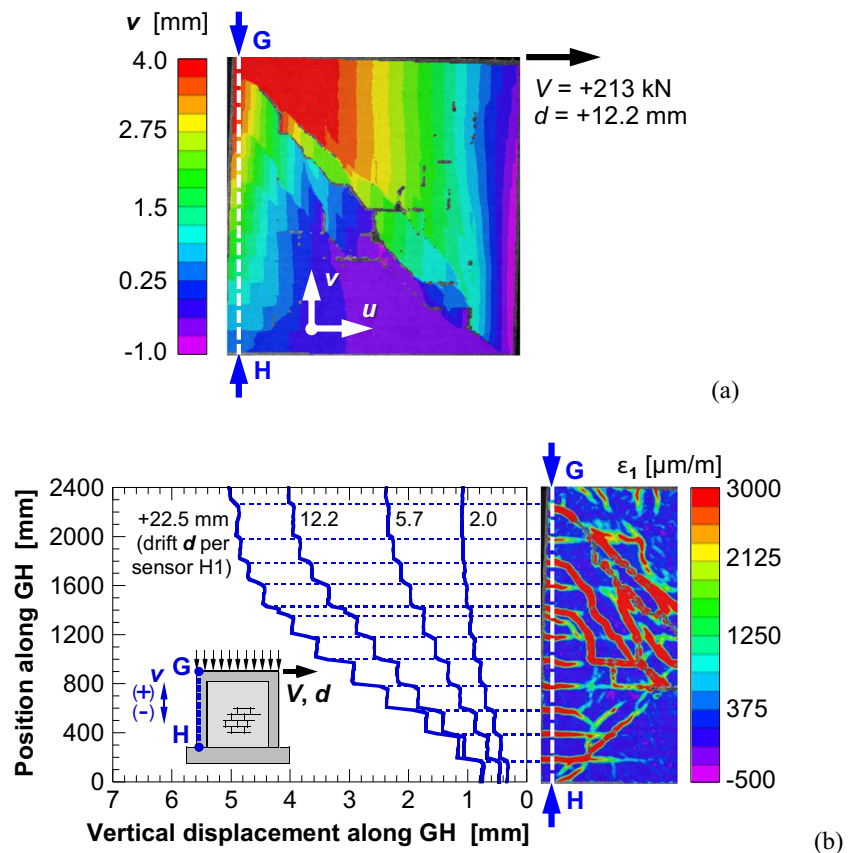
Conclusions

Based on the evidence presented from load tests and 3D-DIC measurements on full-scale confined masonry walls, the following conclusions are drawn.

1. Suitable high-contrast speckle patterns can be applied on large masonry and concrete surfaces by spraying dark paint on flexible stencils. Whitewash can be used to provide a light background.
2. Wide-angle camera lenses are typically needed to capture images of a full-scale masonry wall specimen. Relatively small stereo angles (e.g., 10°) are sufficient when minimal out-of-plane motions are expected, which is typically the case for structural walls loaded horizontally in their plane.
3. It is feasible to define a subset size for 3D-DIC analysis that yields accurate displacement measurements as well as high-resolution crack maps.
4. 3D-DIC measurements of story drift and diagonal deformation offer comparable accuracy to surface-mounted PWSs. To the best of the writers' knowledge, this study is the first to sistematically assess 3D-DIC measurements on large masonry structures vis-à-vis benchmark PWS measurements. Further research is necessary to test the hypothesis that hysteretic load-drift responses can be traced based on 3D-DIC measurements with comparable accuracy to PWSs, and without the need to introduce constant-displacement plateaus in the displacement-control loading history.
5. 3D-DIC measurements of interface slip can be used instead of those from PWSs, which are sensitive to random flexural cracks in the vicinity of the PWS connections to the specimen surface. 3D-DIC displacement fields offer a far more versatile analysis tool as the slip can be assessed virtually anywhere along the masonry-RC interface.
6. Specific strain components can be rendered in 3D-DIC maps to visualize load-resistance mechanisms and failure modes. By using diagonal strain maps, experimental evidence of the development of diagonal struts in CM walls was presented for three specimens with different in-plane strength and deformability. To the best of the writers' knowledge, this study is the first to present the experimental full-field visualization of strut-and-tie mechanisms in masonry infills.
7. Faithful crack maps can be obtained based on 3D-DIC maximum principal strain maps. This method offers significant advantages over hand-drawn maps, including improved level of detail, minimized influence of human errors, ability to map cracks at any loading stage, and safety.
8. Cracks can be accurately located and their progressive opening can be monitored based on 3D-DIC displacement measurements. Further research is necessary to test the hypothesis that the amplitude of the discontinuities in full-field displacement maps can be used to determine crack widths.
9. The 3D-DIC analyses presented herein were performed using a standard desktop PC. Therefore, non-contacting 3D-DIC measurements stand as a powerful and accessible tool to advance the understanding of the behavior of concrete and masonry structures, inform their analysis and design, and underpin the verification and calibration of numerical models. In perspective, there is value and potential in exploring the integration of high-speed stereo-vision systems into novel hybrid testing platforms for structures under dynamic (e.g., seismic, wind) loads. For the specimens discussed in this paper, full-field strain maps provided quantitative and visual evidence on the importance of different design details to enable the development of an effective strut-and-tie and shear resisting mechanism (e.g., corner joint reinforcement vis-à-vis toothed masonry-RC interfaces), and the contribution to shear strength and crack-control of bed-joint reinforcement in a representative strengthened wall (to be used to optimize reinforcement amount and location).

References

1. Voon KC, Ingham JM (2006) Experimental in-plane shear strength investigation of reinforced concrete masonry walls. J Struct Eng 132: 400–408
2. Tena-Colunga A, Juárez-Ángeles A, Salinas-Vallejo VH (2009) Cyclic behavior of combined and confined masonry walls. Eng Struct 31:240–259
3. Shedid MT, El-Dakhakhni WW, Drysdale RG (2009) Behavior of fully grouted reinforced concrete masonry shear walls failing in flexure: analysis. Eng Struct 31:2032–2044
4. Sutton MA, Orteu J-J, Schreier HW (2009) Image correlation for shape, motion and deformation measurements. Springer, New York
5. Sutton MA (2013) Computer vision-based, non-contacting deformation measurements in mechanics: a generational transformation. Appl Mech Rev 65:050000-1-23

6. Lecompte D, Smits A, Bossuyt S, Sol H, Vantomme J, Van Hemelrijck D, Habraken AM (2006) Quality assessment of speckle patterns for digital image correlation. Opt Laser Eng 44:1132–1145

7. Zhou P, Goodson KE (2001) Subpixel displacement and deformation gradient measurement using digital image/speckle correlation (DISC). Opt Eng 40:1613–1620

8. Bornert M, Brémand F, Doumalin P, Dupré J-C, Fazzini M, Grédiac M, Hild F, Mistou S, Molimard J, Orteu J-J, Robert L, Surrel Y, Vacher P, Wattrisse B (2009) Assessment of digital image correlation measurement errors: methodology and results. Exp Mech 49:353–370

9. Ghorbani R, Matta F, Sutton MA (2014) Full-field displacement measurement and crack mapping on masonry walls using digital image correlation. Proc. 2013 SEM Annual Conference – Advancement of Optical Methods in Experimental Mechanics, Springer, 3:187–196

10. Ke XD, Schreier HW, Sutton MA, Wang YQ (2011) Error assessment in stereo-based deformation measurements. Exp Mech 51:423–441

11. Yoneyama S, Kitagawa A, Kitamura K, Kikuta H (2006) Lens distortion correction for digital image correlation by measuring rigid body displacement. Opt Eng 45:023602

12. Pan B, Yu L, Wu D, Tang L (2013) Systematic errors in two-dimensional digital image correlation due to lens distortion. Opt Laser Eng 51:140–147

13. Bräuer-Burchardt C (2004) A simple new method for precise lens distortion correction of low cost camera systems. Lect Notes Comput Sci 3175:570–577

14. Carloni C, Subramaniam KV (2010) Direct determination of cohesive stress transfer during debonding of FRP from concrete. Compos Struct 93:184–192

15. Ghiassi B, Xavier J, Oliveira D, Lourenço P (2013) Application of digital image correlation in investigating the bond between FRP and masonry. Compos Struct 106:340–349

16. Fedele R, Scaioni M, Barazzetti L, Rosati G, Biolzi L (2014) Delamination tests on CFRP-reinforced masonry pillars: optical monitoring and mechanical modeling. Cem Concr Compos 45:243–254

17. Lecompte D, Vantomme J, Sol H (2006) Crack detection in a concrete beam using two different camera techniques. Struct Health Monit 5:59–68

18. Küntz M, Jolin M, Bastien J, Perez F, Hild F (2006) Digital image correlation analysis of crack behavior in a reinforced concrete beam during a load test. Can J Civ Eng 33:1418–1425

19. Destrebecq J-F, Toussaint E, Ferrier E (2011) Analysis of cracks and deformations in a full scale reinforced concrete beam using a digital image correlation technique. Exp Mech 51:879–890

20. Tung S-H, Shih M-H, Sung W-P (2008) Development of digital image correlation method to analyse crack variations of masonry wall. Sadhana 33:767–779

21. Smith BJ, Kurama YC, McGinnis MJ (2010) Design and measured behavior of a hybrid precast concrete wall specimen for seismic regions. J Struct Eng 137:1052–1062

22. Guerrero N, Martínez M, Picón R, Marante ME, Hild F, Roux S, Flórez-López J (2014) Experimental analysis of masonry infilled frames using digital image correlation. Mater Struct 47:873–884

23. Meli R, Brzev S, Astroza M, Boen T, Crisafulli F, Dai J, Farsi M, Hart T, Mebarki A, Moghadam AS, Quiun D, Tomaževič M, Yamin L (2011) Seismic design guide for low-rise confined masonry buildings. Earthquake Engineering Research Institute, Oakland

24. Polyakov SV (1956) Masonry in framed buildings (An investigation into the strength and stiffness of masonry infilling). Gosudarstvennoe Izdatelstvo Literatury po Stroitelstvo i Arkhitekture, Moscow, Russia (English translation by GL Cairns)

25. Holmes M (1961) Steel frames with brickwork and concrete infilling. Proc ICE 19:473–478

26. Tomaževič M (2006) Earthquake resistant design of masonry buildings. Imperial College Press, London

27. Paulay T, Priestley MJN (1992) Seismic design of reinforced concrete and masonry buildings. Wiley, New York